Supporting Information

Spray-Coated Halloysite-Epoxy Composites: a Means to Create Mechanically Robust, Vertically Aligned Nanotube Composites

Kenan Song [†], *Roberta Polak* [†], *Dayong Chen* [†], *Michael F. Rubner* [‡,*], *Robert E. Cohen* [§,*], *Khalid A. Askar* [◊,*]

[†] Department of Materials Science and Engineering, Department of Chemical Engineering, and Department of Mechanical Engineering, MIT, 77 Mass Ave, Cambridge, MA, USA, 02139.

[‡,*] TDK Professor of Polymer Materials Science and Engineering, and Director of CMSE, MIT, 77 Mass Ave, Cambridge, MA, USA, 02139. Correspondence email: rubner@mit.edu

[§,*] St. Laurent Professor of Chemical Engineering Department, MIT, 77 Mass Ave, Cambridge, MA, USA, 02139. Correspondence email: recohen@mit.edu

[◊,*] Department of Materials Science and Engineering, Masdar Institute of Science and Technology, Abu Dhabi, United Arab Emirates. Correspondence email: kaskar@masdar.ac.ae

SI. Viscosity measurements from rheometer

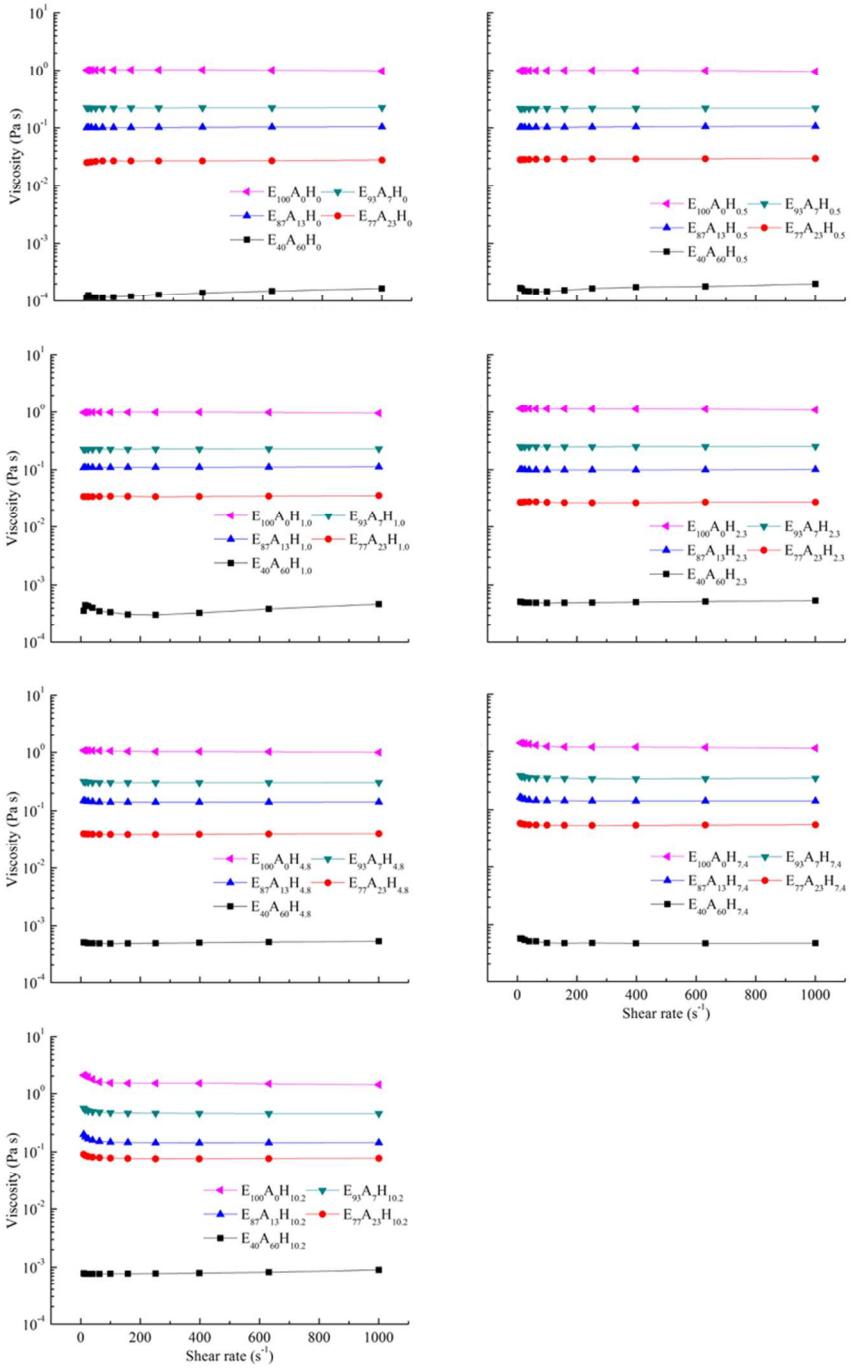

Figure S**1**. Viscosity *vs.* shear rate for HNT suspensions in $E_{40}A_{60}$, $E_{77}A_{23}$, $E_{87}A_{13}$, $E_{93}A_7$ and $E_{100}A_0$, showed an increasing viscosity trend with higher epoxy content. The concentration of HNTs in each figure remains constant. The particle concentration only slightly affects the viscosity compared to the significant change caused by the percentage

of epoxy added. The shear rates in the rheometer measurements are from 10 to 1000 s^{-1} and the temperature is set at 23 ^{o}C.

SII. Relaxation time for nanotubes in fluids

Shear-aligned halloysite nanotubes were sprayed on a glass slide. The alignment of nanotubes is constrained by the epoxy and given enough time the nanotubes would lose their alignment and reach a state of relaxation. The tilted angle and rate depend on particle features (i.e., length, density, shape), and liquid characteristics (i.e., viscosity, temperature, pressure)[1]. The fluid consisting of either pure epoxy or different epoxy/acetone mixtures all displayed Newtonian behavior, as shown in Figure S2. The orientation of the body would eventually be determined by inertia[1]. Bodies with force and front-end symmetry were torque free when settling in Stokes flow, so that the torques due to inertia were unopposed. This resulted in an eventual out-of-plane orientation for all particles[1].

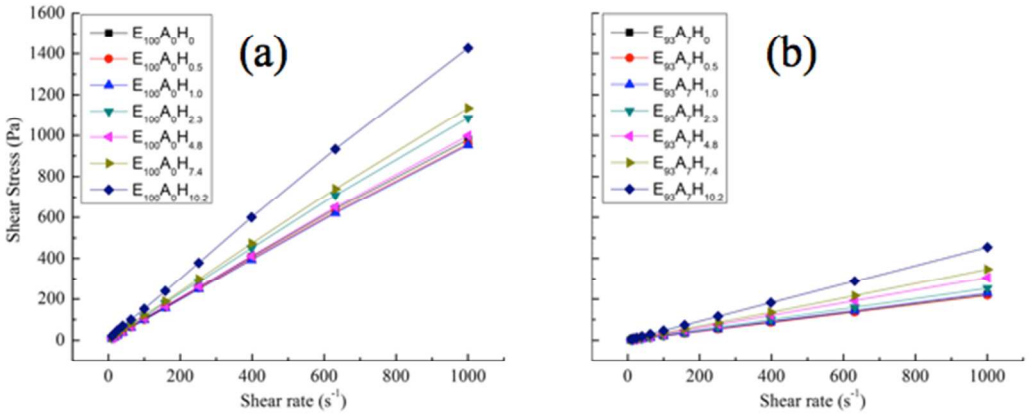

Figure S**2**. Shear stress as a function of shear rates for (a) $E_{100}A_0$ and (b) $E_{93}A_7$ based composites. Linear trends between shear force and shear rate are observed, which exhibits the characteristic of Newtonian fluids. $E_{87}A_{13}$, $E_{77}A_{23}$ and $E_{40}A_{60}$ display the same Newtonian liquid behavior due to the increase in acetone concentration.

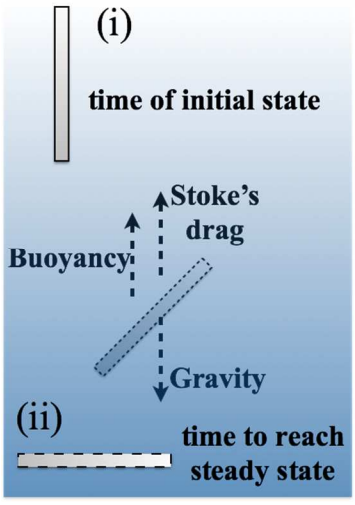

Figure S**3**. Schematic shows the single halloysite nanotube states of (i) as-ejected into the coating surface, and (ii) reaching steady state, and micromechanics model. Relative flow motion past a falling particle in a fluid (i.e., a halloysite nanotube falling through the epoxy solution or melt) generates drag force, F_d, force due to gravity, F_g, as well as buoyancy, F_b.

The sedimentation of the tubes until reaching steady state is equivalent to the steady flow past a stationary long body of halloysite. To simplify the problem, the micromechanics analysis model for a single HNT particle (i.e., diameter of 40 nm and length of 2 μm) falling in a viscous fluid (i.e., viscosity taken from Figure 4) was plotted in Figure S3. The time for the tube to reach steady in-plane state was calculated based on this micromechanics model (Figure S3).

According to Stoke's Law, the force of viscosity on a small particle moving through a viscous fluid is given by[2],

$$F_d = 6\pi\mu R v \qquad \text{(Equation S1)}$$

where F_d is the friction force, known as Stoke's drag, acting on the interface between the fluid and particle. μ is the dynamic viscosity. The liquid states studied here are all Newtonian fluids. Viscosity values were taken as a constant from experimental measurements. R is the quasi-radius of the object. v is the flow velocity relative to the object.

The single particle sedimentation procedure was analyzed by the equation of motion,

$$\begin{aligned} F_{\text{sedimentation}} &= m\dot{v} \\ &= F_d - (F_g - F_b) \\ &= 6\pi\mu R v - (\rho_{particle} - \rho_{fluid}) \cdot g \cdot \frac{4}{3}\pi R^3 \end{aligned} \qquad \text{(Equation S2)}$$

where $\rho_{particle}$ and ρ_{fluid} are the density values of the particle and the fluid, respectively, and g is the gravitational acceleration.

Integrating both sides of Equation S2 gives,

$$\begin{aligned} \int_{t_0}^{t_\infty} m\dot{v}\, dt &= m(v_\infty - v_0) \\ &= \int_{t_0}^{t_\infty} [6\pi\mu R v - (\rho_{particle} - \rho_{fluid}) \cdot g \cdot \frac{4}{3}\pi R^3]\, dt \\ &= \int_{t_0}^{t_\infty} [6\pi\mu R v]\, dt - \int_{t_0}^{t_\infty} [(\rho_{particle} - \rho_{fluid}) \cdot g \cdot \frac{4}{3}\pi R^3]\, dt \end{aligned} \qquad \text{(Equation S3)}$$

To calculate the stability time, t_∞, parameters of v_0 and v_∞ are needed. The initial injection velocity, v_0, can be obtained,

$$v_0 t_{spray} \cdot \pi r_{gun}^2 = V_{spray} \quad \text{(Equation S4)}$$

where t_{spray} is the time consumed for spraying a specific fluidic volume V_{spray}, and r_{gun} is radius of the spraying gun nozzle.

At the equilibrium state, the excess forces of gravity and buoyancy will balance the Stoke's drag force,

$$F_d = F_g - F_b = (\rho_{particle} - \rho_{fluid}) \cdot g \cdot \frac{4}{3} \pi R^3 \quad \text{(Equation S5)}$$

The resulting equilibrium velocity, v_∞, can be calculated via combining Equations S1 and S5,

$$v_\infty = \frac{2}{9} \frac{(\rho_{particle} - \rho_{fluid})}{\mu} \cdot g \cdot R^2 \quad \text{(Equation S6)}$$

Taking all the equations above, the calculated particle settling time was plotted in Figure S4.

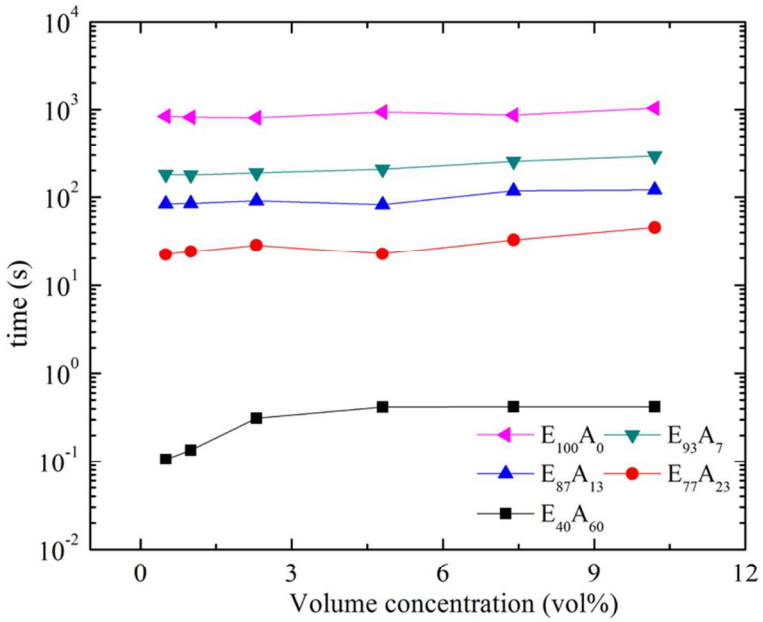

Figure S**4**. Relaxation time from vertical to horizontal alignment for a single particle (i.e., diameter of 40 nm and length of 2 μm and viscosity values at shear rate of 631 s^{-1} were taken from Figure 4) in various viscous fluids used in this research

SIII. Literature research of epoxy composites mechanical properties as compared to this study

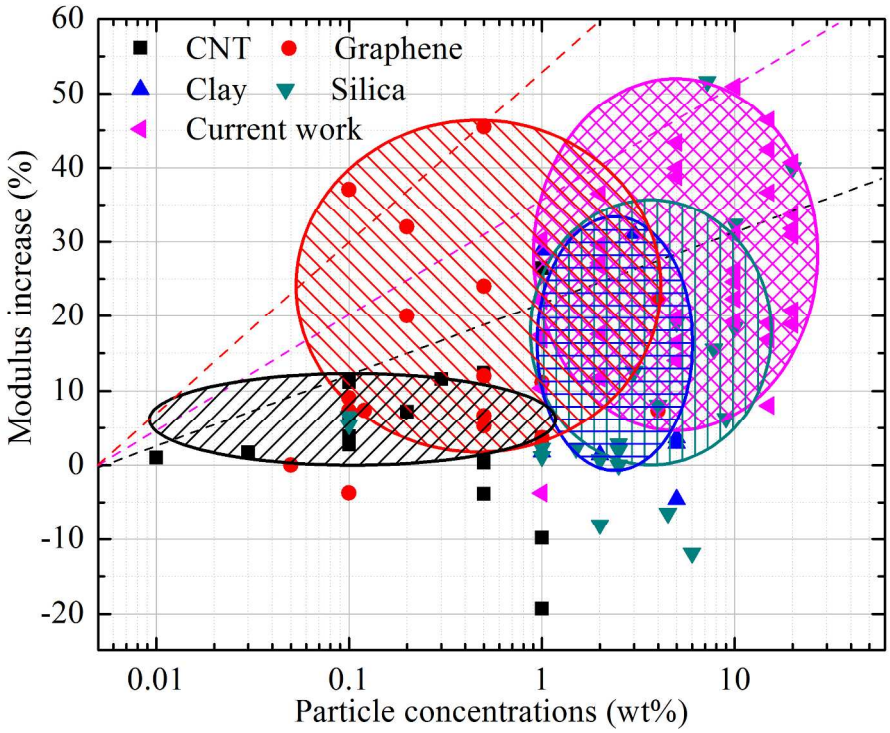

Figure S**5**. Ashby Chart of modulus increase (i.e., %, $(E_{composite}-E_{epoxy})/E_{epoxy}$) of nanoparticles/epoxy composites *vs.* particle concentrations. Carbon nanotubes [3-13], graphene [14-25], montmorillonitrile clay [26-30], silica [31-42], and current work data has been plotted. Tilted lines stand for specific modulus increase in percentage, and the slopes indicate reinforcement in modulus per unit particle concentration. It can be seen that the current work showed intermediate reinforcement efficiency between graphene and carbon nanotubes; however, HNTs cost is $2/kg, while carbon nanotubes and graphene price range from $50/g to $500/g[43]. The current work also achieves modulus increases beyond that from frequently used particles of montmorillonite and silica. The secret is in the particle alignment along loading direction.

SIV. Composite mechanics

TGA experiments were used to confirm the concentrations of HNT in the final processed composites. Data of this type is compared in Figure 6a with the nominal HNT compositions, based on formulation compounding. It can be seen that the final composite concentrations are very consistent with the designed loadings (Figure 6b). This also validates a stable distribution of HNTs in the various viscous spray-processing formulations, where epoxy/acetone ratios vary considerably. Macroscopic sedimentation

was not observed even in 10.2 vol% HNT loadings.

In Cox-Krenchel model[44], length efficiency factor was defined,

$$\eta_l = 1 - [\frac{\tanh(na)}{na}] \quad \text{(Equation S7)}$$

$$n = \sqrt{[\frac{2G_m}{E_f \ln(2R/d)}]} \quad \text{(Equation S8)}$$

$$a = \frac{l}{d} \quad \text{(Equation S9)}$$

where G_m is the shear modulus of polymer matrix, $2R$ is the distance from the fiber to its nearest neighbor fiber, l and d mean the length and diameter of the particle.

At fixed fiber concentration below percolation (i.e., less than 1 vol% in our HNT nanocomposites) and under uniform dispersion, length efficiency is only dependent on aspect ratio and concentration as shown in Equations S7 to S9. Figure S6c shows how the length efficiency factor changes with lumped parameter *na,* and the insert demonstrates how *na* changes with volume concentrations. Based on this curve from Equation S7, as well as the parameters including ① shear modulus of 1.7 GPa for epoxy as calculated from the experimentally determined Young's modulus (4.5 GPa), ② Poisson's ratio (0.3), ③tensile modulus for HNTs of 300 GPa[45-46], and ④ HNTs concentration of 0.5 vol.% generate a value of 5 for *na*. This corresponds to a length efficiency of 81% in Figure S6c. In this study, the HNT volume fractions, V_f, varied from ~0.5 vol% to ~10.2 vol%, indicating the matrix volume fractions, V_m, from ~99.5 vol% to ~89.8 vol%. This change in concentration, however, does not change the length efficiency factor significantly, with η_l ranges from 81% to 86% (insert in Figure S6c). Therefore, the analysis of orientation efficiency factor will reveal their main influencing effectiveness on mechanical properties as discussed in the manuscript.

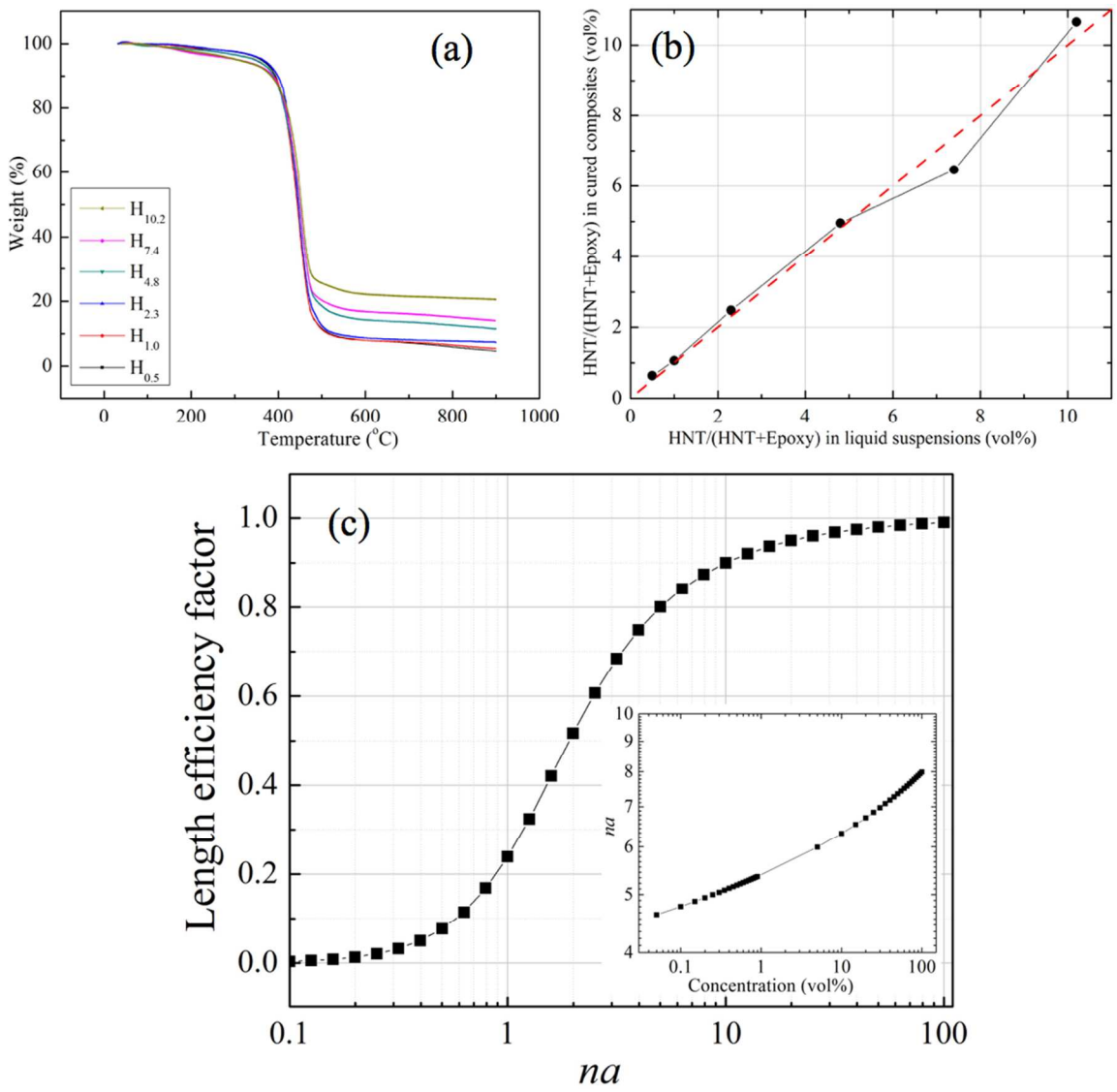

Figure S6 (a) TGA of composites with various HNT concentrations, and (b) the relationship of HNT concentration between experimental design and actual values in the final cured composites showed consistency. (c) Length efficiency factor (η_l) as a function of parameter *na*.

SV. Orientation of HNT based on composite mechanics

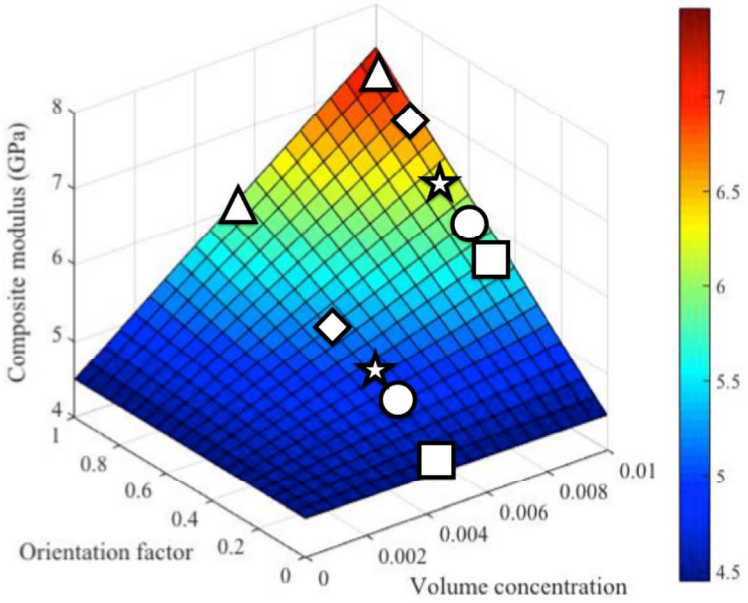

Figure S**7** Contour of composite elastic modulus from Cox-Krenchel model with orientation factor and volume fraction variations. Composite moduli at various volumes (i.e., 0.5 vol% and 1.0 vol%) showed the orientation factor trend distinctively. Composites based on $E_{40}A_{60}$ (O), $E_{77}A_{23}$ (□), $E_{87}A_{13}$ (☆), $E_{93}A_{7}$ (Δ), and $E_{100}A_{0}$ (◊) are marked.

The orientation factor can also be calculated based on composite mechanics. The spin-coating method produces a film with randomly orientated particles with an orientation factor η_o of 0.2[47]. A linear fitting of the experimental modulus values between 0 and 1 vol% in spin-coated films gives effective modulus of HNT of ~312 GPa (i.e., moduli of 5.20, 5.74, and 5.81 GPa at HNT concentrations of 0, 0.5, and 1.0 vol%). At a rough estimation, E_m =4.5 GPa and E_f=312 GPa, the composite modulus relative to orientation factor (i.e., 0 to 1) and fiber volume fraction (i.e., 0 to 1 vol%) is plotted in Figure S7. The spray-coated samples were shown as white symbols on the contour so that their orientation factors at specific volumes of 0.5 vol% and 1.0 vol% become straightforward. The orientation factors showed consistent increase with viscosity values. Figure S7 shows that with a specific volume fraction, better consistency in particle orientation results in high modulus values. In spite of this relationship between orientation factor and modulus values, composite mechanics is not a straightforward method for particle orientation calculations. Therefore statistical quantifications of HNT orientations in these composites are important and have been given in the manuscript discussion sections.

Table S**1**. Orientation factors calculated from composite mechanics

Samples	Orientation factors based on composite mechanics				
	$E_{40}A_{60}$	$E_{77}A_{23}$	$E_{87}A_{13}$	$E_{93}A_{7}$	$E_{100}A_{0}$
0.5 (vol%)	0.38	N/A	0.46	0.97	0.69
1.0 (vol%)	0.72	0.68	0.81	1.00	0.96

SVI. Analyses of HNTs alignment based on SEM images

Table S**2**. Gaussian fitting of halloysite orientations in composite coatings

Sample		Fitted Gaussian equation parameters	
Solution components	HNTs Concentration (vol%)	A	FWHM
$E_{77}A_{23}$	0.5	426.72	28.71
	1.0	477.15	49.47
	4.8	413.50	26.55
	10.2	451.45	22.49
$E_{93}A_{7}$	0.5	504.60	96.76
	1.0	484.29	66.70
	4.8	496.07	70.93
	10.2	458.86	65.17
$E_{100}A0$	0.5	497.18	58.83
	1.0	474.18	44.40
	4.8	468.66	26.37
	10.2	425.74	15.56

Note: Gaussian fitting of $y = y_0 + \frac{Ae^{\frac{-4\ln(2)(x-x_c)^2}{w^2}}}{w\sqrt{\frac{\pi}{4\ln(2)}}}$, *where* $y_c=y_0+A/(FWHM*sqrt(\pi/4ln2))$, *FWHM* is the full width at half maximum and *A* is the area integrated. y_0 is base, x_c stands for the fitted peak center which is 0^o for out-of-plane aligned particles and 90^o for in-plane aligned particles. The script access of the function is nlf_Gaussian(x,y0,xc,A,w).

SVII. Intrinsic modulus for halloysite

Table S**3.** Mechanics of HNT from literature and current work

Report	Test method	Parameters
2005[48]	First principle study using molecular dynamics simulations	Kaolinite with halloysite composition shows Young's modulus of 170 GPa along tube direction
2010[45]	Simulation using self-consistent charge density-functional based tight-binding (SCC-DFTB) method	Single-wall HNT posses moduli between 234 and 339 GPa with diameters ranging from 1.7 to 4.6 nm
2011[49]	TEM observed cantilever beam bending tests	Bending moduli ranges from 60 to 156 GPa dependent on radius from 16 to 70 nm
2013[46]	Three-point bending tests performed on individual nanotubes using an AFM tip	The calculated average elastic modulus ranges from average 10 to 600 GPa, with a diameter-normalized value of 140 GPa, measured for a set of tubes with outer diameters ranging between 50 and 160 nm.

		The highest value reaches around 600 GPa at diameters less than 50 nm.
Current work	Composite mechanics	Reinforcement modulus without considering misalignment effects reached as high as 182 GPa and HNT intrinsic modulus was predicted to be around 420 GPa

SVIII. Percolation threshold analyses

HNT particles have been known for their high modulus, up to around 600 GPa at outer diameters of less than 50 nm. However, as tubes started aggregating, the accumulating defects and the lack of inter-tubular registry resulting from diameter differences and helicity variations will lead to decrease of effective modulus, especially shear modulus. For example, carbon nanotubes have been shown to have shear modulus of 6 GPa for 4.5 nm bundles, 2.3 GPa for 9 nm bundles and 0.7 GPa for 20 nm bundles [50-52]. Therefore a theoretical estimation of the average modulus dependent on bundle size will be necessary to understand the plateau region in Figure 9. The average effective modulus $<E_x>$ has been calculated using continuum mechanics (Equation S10)[47]. Modulus along longitudinal direction (E_1), transverse direction (E_2), and Poisson's ratio (ν) were from Table 4 and also listed in Figure 9d. Shear modulus (G_{12}) dependent on bundles size is not available experimentally; here in this research were taken as 2, 5, 10, and 20 GPa to show the average modulus change with bundle size[53]. The existence of plateau region can be attributed to two aspects. (i) From Figure 9d, it can be seen that with the bundle size increase, the decrease in effective average modulus can be one order of magnitude lower. In addition, for the same bundle size, the average modulus was also found to improve with higher alignment. This is also consistent with the phenomenon as indicated from the trend line in Figures 8a and 8b. (ii) The bundled structure not only influences the intrinsic particle modulus and hardness values but also affect the interaction between polymers and particles. Fully dispersed and exfoliated nanotubes will have more contact area than aggregates, and reinforcement efficiency has also been found to be linearly proportional to interfacial area[54]. This could be another reason for the formation of plateau.

$$\frac{1}{<E_x>}=\frac{<\cos^4\theta>}{E_1}+\frac{<\sin^4\theta>}{E_2}+\left(\frac{1}{G_{12}}-\frac{2\nu_{12}}{E_1}\right)<\cos^2\theta\cos^2\theta>$$
$$=\frac{1}{E_2}+\left(\frac{1}{G_{12}}-\frac{2\nu_{12}}{E_1}-\frac{2}{E_2}\right)<\cos^2\theta>+\left(\frac{1}{E_1}+\frac{1}{E_2}-\frac{1}{G_{12}}+\frac{2\nu_{12}}{E_1}\right)<\cos^4\theta> \quad \text{(Equation S10)}$$

References

1. Liu, Y. J.; Joseph, D. D., Sedimentation of Particles in Polymer Solutions. *J. Fluid Mech.* **1993,** *255*, 565-595.
2. Munson, B. R.; Young, D. F.; Okiishi, T. H., *Fundamentals of Fluid Mechanics*. 2nd ed.; John Wiley & Sons, Inc: New York US, **1990**; Vol. 3, p 4-40.
3. Gojny, F. H.; Wichmann, M. H. G.; Fiedler, B.; Schulte, K., Influence of Different Carbon Nanotubes on the Mechanical Properties of Epoxy Matrix Composites – a Comparative Study. *Compos. Sci. Technol.* **2005,** *65*, 2300-2313.

4. Sun, L.; Warren, G. L.; O'Reilly, J. Y.; Everett, W. N.; Lee, S. M.; Davis, D.; Lagoudas, D.; Sue, H. J., Mechanical Properties of Surface-Functionalized Swcnt/Epoxy Composites. *Carbon* **2008,** *46*, 320-328.
5. Gojny, F.; Wichmann, M.; Köpke, U.; Fiedler, B.; Schulte, K., Carbon Nanotube-Reinforced Epoxy-Composites: Enhanced Stiffness and Fracture Toughness at Low Nanotube Content. *Compos. Sci. Technol.* **2004,** *64*, 2363-2371.
6. Ayatollahi, M. R.; Shadlou, S.; Shokrieh, M. M., Fracture Toughness of Epoxy/Multi-Walled Carbon Nanotube Nano-Composites under Bending and Shear Loading Conditions. *Mater. Des.* **2011,** *32*, 2115-2124.
7. Ayatollahi, M. R.; Shadlou, S.; Shokrieh, M. M., Mixed Mode Brittle Fracture in Epoxy/Multi-Walled Carbon Nanotube Nanocomposites. *Eng. Fract. Mech.* **2011,** *78*, 2620-2632.
8. Young, R. J.; Kinloch, I. A.; Gong, L.; Novoselov, K. S., The Mechanics of Graphene Nanocomposites: A Review. *Compos. Sci. Technol.* **2012,** *72*, 1459-1476.
9. Gkikas, G.; Barkoula, N. M.; Paipetis, A. S., Effect of Dispersion Conditions on the Thermo-Mechanical and Toughness Properties of Multi Walled Carbon Nanotubes-Reinforced Epoxy. *Composites, Part B* **2012,** *43*, 2697-2705.
10. Tang, L.-c.; Zhang, H.; Han, J.-h.; Wu, X.-p.; Zhang, Z., Fracture Mechanisms of Epoxy Filled with Ozone Functionalized Multi-Wall Carbon Nanotubes. *Compos. Sci. Technol.* **2011,** *72*, 7-13.
11. Karapappas, P.; Vavouliotis, A.; Tsotra, P.; Kostopoulos, V.; Palpetis, A., Enhanced Fracture Properties of Carbon Reinforced Composites by the Addition of Multi-Wall Carbon Nanotubes. *J. Compos. Mater.* **2009,** *43*, 977-985.
12. Hsieh, T. H.; Kinloch, A. J.; Taylor, A. C.; Kinloch, I. A., The Effect of Carbon Nanotubes on the Fracture Toughness and Fatigue Performance of a Thermosetting Epoxy Polymer. *J. Mater. Sci.* **2011,** *46*, 7525-7535.
13. Hsieh, T.; Kinloch, A.; Taylor, A.; Sprenger, S., The Effect of Silica Nanoparticles and Carbon Nanotubes on the Toughness of a Thermosetting Epoxy Polymer. *J. Appl. Polym. Sci.* **2011,** *119*, 2135-2142.
14. Liu, Y.; Wu, H.; Chen, G., Enhanced Mechanical Properties of Nanocomposites at Low Graphene Content Based on in Situ Ball Milling. *Polym. Compos.* **2014,** *37*, 1190-1197.
15. Tang, L.-C.; Wan, Y.-J.; Yan, D.; Pei, Y.-B.; Zhao, L.; Li, Y.-B.; Wu, L.-B.; Jiang, J.-X.; Lai, G.-Q., The Effect of Graphene Dispersion on the Mechanical Properties of Graphene/Epoxy Composites. *Carbon* **2013,** *60*, 16-27.
16. Bortz, D. R.; Heras, E. G.; Martin-Gullon, I., Impressive Fatigue Life and Fracture Toughness Improvements in Graphene Oxide/Epoxy Composites. *Macromol.* **2012,** *45*, 238-245.
17. Zaman, I.; Phan, T. T.; Kuan, H.-C.; Meng, Q.; Bao La, L. T.; Luong, L.; Youssf, O.; Ma, J., Epoxy/Graphene Platelets Nanocomposites with Two Levels of Interface Strength. *Polym.* **2011,** *52*, 1603-1611.
18. Zaman, I.; Kuan, H. C.; Meng, Q.; Michelmore, A.; Kawashima, N.; Pitt, T.; Zhang, L.; Gouda, S.; Luong, L.; Ma, J., A Facile Approach to Chemically Modified Graphene and Its Polymer Nanocomposites. *Adv. Funct. Mater.* **2012,** *22*, 2735-2743.
19. Chatterjee, S.; Wang, J. W.; Kuo, W. S.; Tai, N. H.; Salzmann, C.; Li, W. L.; Hollertz, R.; Nüesch, F. A.; Chu, B. T. T., Mechanical Reinforcement and Thermal

Conductivity in Expanded Graphene Nanoplatelets Reinforced Epoxy Composites. *Chem. Phys. Lett.* **2012,** *531*, 6-10.
20. Jiang, T.; Kuila, T.; Kim, N. H.; Ku, B.-C.; Lee, J. H., Enhanced Mechanical Properties of Silanized Silica Nanoparticle Attached Graphene Oxide/Epoxy Composites. *Compos. Sci. Technol.* **2013,** *79*, 115-125.
21. Shokrieh, M. M.; Ghoreishi, S. M.; Esmkhani, M.; Zhao, Z., Effects of Graphene Nanoplatelets and Graphene Nanosheets on Fracture Toughness of Epoxy Nanocomposites. *Fatigue Fract. Eng. Mater. Struct.* **2014,** *37*, 1116-1123.
22. Li, Z.; Wang, R.; Young, R. J.; Deng, L.; Yang, F.; Hao, L.; Jiao, W.; Liu, W., Control of the Functionality of Graphene Oxide for Its Application In epoxy Nanocomposites. *Polym.* **2013,** *54*, 6437-6446.
23. Chandrasekaran, S.; Sato, N.; Tölle, F.; Mülhaupt, R.; Fiedler, B.; Schulte, K., Fracture Toughness and Failure Mechanism of Graphene Based Epoxy Composites. *Compos. Sci. Technol.* **2014,** *97*, 90-99.
24. Ahmadi-Moghadam, B.; Taheri, F., Fracture and Toughening Mechanisms of Gnp-Based Nanocomposites in Modes I and Ii Fracture. *Eng. Fract. Mech.* **2014,** *131*, 329-339.
25. Galpaya, D.; Wang, M.; Liu, M.; Motta, N.; Waclawik, E.; Yan, C., Recent Advances in Fabrication and Characterization of Graphene-Polymer Nanocomposites. *Graphene* **2012,** *1*, 30-49.
26. Qi, B.; Zhang, Q. X.; Bannister, M.; Mai, Y. W., Investigation of the Mechanical Properties of Dgeba-Based Epoxy Resin with Nanoclay Additives. *Compos. Struct.* **2006,** *75*, 514-519.
27. Wang, L.; Wang, K.; Chen, L.; Zhang, Y.; He, C., Preparation, Morphology and Thermal/Mechanical Pproperties of Epoxy/Nanoclay Composite. *Composites, Part A* **2006,** *37*, 1890-1896.
28. Wang, K.; Chen, L.; Wu, J.; Toh, M. L.; He, C.; Yee, A. F., Epoxy Nanocomposites with Highly Exfoliated Clay: Mechanical Properties and Fracture Mechanisms. *Macromol.* **2005,** *38*, 788-800.
29. Zappalorto, M.; Salviato, M.; Quaresimin, M., Mixed Mode (I + Ii) Fracture Toughness of Polymer Nanoclay Nanocomposites. *Eng. Fract. Mech.* **2013,** *111*, 50-64.
30. Guevara-Morales, A.; Taylor, A. C., Mechanical and Dielectric Properties of Epoxy–Clay Nanocomposites. *J. Mater. Sci.* **2013,** *49*, 1574-1584.
31. Tang, L.-C.; Zhang, H.; Sprenger, S.; Ye, L.; Zhang, Z., Fracture Mechanisms of Epoxy-Based Ternary Composites Filled with Rigid-Soft Particles. *Compos. Sci. Technol.* **2012,** *72*, 558-565.
32. Liu, H.-Y.; Wang, G.-T.; Mai, Y.-W.; Zeng, Y., On Fracture Toughness of Nano-Particle Modified Epoxy. *Composites, Part B* **2011,** *42*, 2170-2175.
33. Brunner, A. J.; Necola, A.; Rees, M.; Gasser, P.; Kornmann, X.; Thomann, R.; Barbezat, M., The Influence of Silicate-Based Nano-Filler on the Fracture Toughness of Epoxy Resin. *Eng. Fract. Mech.* **2006,** *73*, 2336-2345.
34. Chen, L.; Chai, S.; Liu, K.; Ning, N.; Gao, J.; Liu, Q.; Chen, F.; Fu, Q., Enhanced Epoxy/Silica Composites Mechanical Properties by Introducing Graphene Oxide to the Interface. *ACS Appl. Mater. Interfaces* **2012,** *4*, 4398-4404.

35. Liang, Y. L.; Pearson, R. A., Toughening Mechanisms in Epoxy–Silica Nanocomposites (Esns). *Polym.* **2009,** *50*, 4895-4905.
36. Zhang, C.; Wang, J.; Du, Y.; Zhang, W., An Investigation on the Thermodynamic Stability of V6si5. *J. Mater. Sci.* **2007,** *42*, 7046-7048.
37. Kinloch, A. J.; Mohammed, R. D.; Taylor, A. C.; Eger, C.; Sprenger, S.; Egan, D., The Effect of Silica Nano Particles and Rubber Particles on the Tughness of Multiphase Thermosetting Epoxy Polymers. *J. Mater. Sci.* **2005,** *40*, 5083-5086.
38. Zamanian, M.; Mortezaei, M.; Salehnia, B.; Jam, J. E., Fracture Toughness of Epoxy Polymer Modified with Nanosilica Particles: Particle Size Effect. *Eng. Fract. Mech.* **2013,** *97*, 193-206.
39. Dittanet, P.; Pearson, R. A., Effect of Silica Nanoparticle Size on Toughening Mechanisms of Filled Epoxy. *Polym.* **2012,** *53*, 1890-1905.
40. Johnsen, B. B.; Kinloch, A. J.; Mohammed, R. D.; Taylor, A. C.; Sprenger, S., Toughening Mechanisms of Nanoparticle-Modified Epoxy Polymers. *Polym.* **2007,** *48*, 530-541.
41. Bray, D. J.; Dittanet, P.; Guild, F. J.; Kinloch, A. J.; Masania, K.; Pearson, R. A.; Taylor, A. C., The Modelling of the Toughening of Epoxy Polymers Via Silica Nanoparticles: The Effects of Volume Fraction and Particle Size. *Polym.* **2013,** *54*, 7022-7032.
42. Ma, J.; Mo, M.-S.; Du, X.-S.; Rosso, P.; Friedrich, K.; Kuan, H.-C., Effect of Inorganic Nanoparticles on Mechanical Property, Fracture Toughness and Toughening Mechanism of Two Epoxy Systems. *Polym.* **2008,** *49*, 3510-3523.
43. Https://Www.Cheaptubes.Com.
44. Cox, H., The Elasticity and Strength of Paper and Other Fibrous Materials. *Br. J. Appl. Phys.* **1952,** *3*, 72-75.
45. Guimaraes, L.; Enyashin, A. N.; Seifert, G.; Duarte, H. A., Structural, Electronic, and Mechanical Properties of Single-Walled Halloysite Nanotube Models. *J. Phys. Chem. C* **2010,** *114*, 11358-11363.
46. Lecouvet, B.; Horion, J.; D'Haese, C.; Bailly, C.; Nysten, B., Elastic Modulus of Halloysite Nanotubes. *Nanotech.* **2013,** *24*, 105704-105711.
47. Song, K.; Zhang, Y.; Meng, J.; Green, E. C.; Tajaddod, N.; Li, H.; Minus, M. L., Structural Polymer-Based Carbon Nanotube Composite Fibers: Understanding the Processing–Structure–Performance Relationship. *Mater.* **2013,** *6*, 2543-2577.
48. Sato, H.; Ono, K.; Johnston, C. T.; Yamagishi, A., First-Principles Studies on the Elastic Constants of a 1: 1 Layered Kaolinite Mineral. *Am. Mineral.* **2005,** *90*, 1824-1826.
49. Lu, D.; Chen, H.; Wu, J.; Chan, C. M., Direct Measurements of the Young's Modulus of a Single Halloysite Nanotube Using a Transmission Electron Microscope with a Bending Stage. *J. Nanosci. Nanotechnol.* **2011,** *11*, 7789-7793.
50. Salvetat, J.-P.; Briggs, G. A. D.; Bonard, J.-M.; Bacsa, R. R.; Kulik, A. J.; Stöckli, T.; Burnham, N. A.; Forró, L., Elastic and Shear Moduli of Single-Walled Carbon Nanotube Ropes. *Phys. Rev. Lett.* **1999,** *82*, 944-947.
51. Satcurada, I.; Ito, T.; Nakamae, K., Elastic Moduli of the Crystal Lattices of Polymers. *J. Polym. Sci., Part C: Polym. Symp.* **1967,** *15*, 75-91.
52. Popov, V.; Van Doren, V.; Balkanski, M., Elastic Properties of Crystals of Single-Walled Carbon Nanotubes. *Solid State Commun.* **2000,** *114*, 395-399.

53. Liu, T.; Kumar, S., Effect of Orientation on the Modulus of Swnt Films and Fibers. *Nano Lett.* **2003,** *3*, 647-650.
54. Cadek, M.; Coleman, J. N.; Ryan, K. P., Reinforcement of Polymers with Carbon Nanotubes:The Role of Nanotube Surface Area. *Nano Lett.* **2004,** *4*, 353-356.